JOURNAL OF THERMOPHYSICS AND HEAT TRANSFER
Vol. 22, No. 2, April–June 2008

Analysis of Segmented Arc-Heater Flows with High Argon Concentration

Jeong-Il Lee,* Sang-Hoon Han,† Chongam Kim,‡ and Kyu-Hong Kim§
Seoul National University, Seoul 151-742, Republic of Korea

DOI: 10.2514/1.33623

The existing computer code to solve the airflow in a segmented constrictor-type arc-heated wind tunnel named ARCFLO4 is improved to accept an air–argon mixture as the working gas. The new version of the code is used to calculate the flows in the Aerodynamic Heating Facility of NASA Ames Research Center where argon concentration is relatively high. The calculation shows that argon tends to increase the diameter of the arc column, increase ionization fraction, decrease thermal efficiency of the arc heater, and push the ratio of the centerline-to-average enthalpy toward unity. The calculated operating characteristics of the arc heater agree well with the experimental data and the results of the calculations made by Sakai using a similar code developed earlier, ARCFLO3.

Nomenclature

$C_{p,i}$ = specific heat of species at constant pressure
c = speed of light
E = voltage gradient
H = total enthalpy
H_a = mass-averaged enthalpy
h = specific enthalpy or Planck constant
I = current
j = current density
k = Boltzmann constant
$\dot{m}$ = mass flow rate
N_A = Avogadro's number
p = pressure
q_c = conductive heat flux
q_n = radiative heat flux at frequency band
q_R = radiative heat flux
q_ν = radiative heat flux at frequency
R = radius of the constrictor or universal gas constant
r = radial coordinate
T = temperature
u = axial velocity
V = voltage
x = axial coordinate
y = radial coordinate
α = angle in cross-sectional plane from radial direction to projected line of sight
η = arc-heater efficiency
θ = angle between the ray and the outward normal to the cylindrical surface
ν = radiation frequency
ρ = density
σ = electrical conductivity
Ω = solid angle

Received 21 July 2007; revision received 28 December 2007; accepted for publication 3 January 2008.

*Postdoctoral Fellow, School of Mechanical and Aerospace Engineering, Sillim-Dong, Gwanak-Gu; snow0730@empal.com. Member AIAA.

†Graduate Research Assistant, School of Mechanical and Aerospace Engineering, Sillim-Dong, Gwanak-Gu; airshhan@naver.com. Member AIAA.

‡Associate Professor, School of Mechanical and Aerospace Engineering and Institute of Advanced Aerospace Technology, Sillim-Dong, Gwanak-Gu; chongam@snu.ac.kr. Senior Member AIAA.

§Assistant Professor, School of Mechanical and Aerospace Engineering and Institute of Advanced Aerospace Technology, Sillim-Dong, Gwanak-Gu; aerocfd1@snu.ac.kr; Member AIAA (Corresponding Author).

I. Introduction

AN ARC heater is a device that produces high enthalpy flow for a long time and is usually used to study aerodynamic heating in ground tests. Among several types of arc heaters, the segmented type arc heaters can produce a stable flow under wide range conditions, which is an essential requirement for ground experiments. Generally, the flow in a segmented type arc heater is a complex plasma flow, which is heated directly by the arc. The flow experiences a strong energy transfer from its core to the surrounding gas mainly by radiation and turbulent mixing. Many numerical and experimental investigations have been carried out to elucidate the flow physics.

The present paper is also one of theoretical and numerical efforts to investigate the flow physics in an arc heater. Historically, Nicolet et al. [1] developed the ARCFLO code based on the work of Waston and Pegot [2]. It adopts a two-band radiation model that accounts for self-absorption and a Cebeci–Smith [3] algebraic turbulence model. This code can reasonably predict the overall operating characteristics of existing arc heaters. However, the applicability of the ARCFLO code was quite restrictive in the step of the actual design or development of the arc heaters because it employed the space marching technique, which requires upstream conditions in advance. Therefore, to overcome this shortcoming, Kim et al. [4] developed a time marching code, ARCFLO2, which solves the time-dependent Navier–Stokes equations. They retained the two-band radiation model and Cebeci–Smith algebraic turbulence model from the ARCFLO code. All the properties were computed successfully only with the geometry of the arc heater and the given operating conditions, that is, the current and the mass flow rate. Subsequently, Sakai and Olejniczak [5–8] also tried to improve ARCFLO2. They developed a new three-band radiation model, which was consistent with a detailed line-by-line calculation; this code is named ARCFLO3. However, ARCFLO3 as well as ARCFLO2 does not always produce acceptable numerical accuracy for the various arc heaters over a wide range of operating conditions. Recently, the authors [9–11] developed an improved numerical code, ARCFLO4, which can be applied to the various arc heaters under arbitrary operating conditions. Instead of a conventional algebraic turbulence model, we adopted a two-equation turbulence model, which is able to express the convective physics of turbulence and does not explicitly demand a mixing length. Also, the three-band radiation model of ARCFLO3, whose performance and numerical accuracy were proven by Sakai and Olejniczak [6], was used. It was observed that the k–ε turbulence model [12] combined with the three-band radiation model provided very good solutions over diverse operating conditions.

However, in some regions, especially under the low mass flow rate condition of the Aerodynamic Heating Facility (AHF), the accuracy of mass-averaged enthalpy was not satisfactory. Particularly, a qualitatively different trend was observed between experiments and ARCFLO4 in the case of the mass-averaged enthalpy. Among the several possibilities for this difference in the trend, the negligence of argon injection from the electrode region was suspected as the primary reason. Generally, a small amount of argon gas, for example, about 0.03 kg/s in the AHF [13] and 0.04 kg/s in the Interaction Heating Facility (IHF) [13] at the NASA Ames Research Center, is injected from the electrode region to ensure that sufficient ionization is maintained near the surface of the electrodes. However, this was ignored in our previous studies [9–11] because the mass flow rate of air was large enough in most test cases. Accordingly, it is probable that solutions were affected by the small amount of argon gas when the mass flow rate of air was below 0.1 kg/s, that is, when the order of the mass flow rate of air became comparable to that of argon.

The present study focused on the influence of the air–argon mixture on the behavior and the accuracy of the solution. To analyze the flows of the air–argon mixture, the thermodynamic and transport properties of the air–argon mixture were calculated under the assumption of the thermal equilibrium condition. Then, the properties were applied to the 20-MW AHF at the NASA Ames Research Center, combined with the Joule heating model of ARCFLO, the k–ε turbulence model, and the three-band radiation model. This paper is organized as follows: Sec. I is the Introduction; Sec. II briefly describes the numerical and physical modeling such as numerical approaches, equilibrium composition, thermodynamic and transport properties, a Joule heating model, a radiation model, and a turbulence model. In the results section, Sec. III, the AHF operation is simulated to verify the performance of the proposed numerical models, and the role of the argon gas is investigated. Finally, concluding remarks are presented in Sec. IV.

II. Numerical Modeling

A. Numerical Approaches

Figure 1 shows a segmented constrictor-type arc heater. It consists of an anode chamber, a constrictor, a cathode chamber, and a nozzle. Most of the test gases are injected through the wall of the constrictor and exited through the nozzle into the test section. In the constrictor, the arc spans between the two electrodes. The core gas is heated by arc's Joule heating. The surrounding gas is heated by radiation emitted from the core gas and by turbulent mixing. Heat energy arriving at the constrictor wall is removed by the cooling water which circulates through the constrictor disks.

Based on our previous studies [9–11], the governing equations are the time-dependent axisymmetric Navier–Stokes equations, which include Joule heating by arc, radiation, and turbulence. The governing equations are then discretized by the finite volume method. The inviscid flux is given by the AUSMPW+ [14] scheme. The viscous flux is calculated through a central difference scheme. The inviscid term is handled implicitly by applying the lower–upper symmetric Gauss–Seidel (LU-SGS) [15] method. The axisymmetric source, Joule heating, and the viscous term are calculated explicitly.

The computational grid which is scaled up to 10 times in the radial direction is shown in Fig. 2. The AHF arc heater has a constrictor diameter of 0.06 m and length of 2.3 m. The nozzle throat diameter is 0.038 m. The dimensions of the constrictor and nozzle throat were directly obtained from [6]. The geometry of the electrode chambers which was not explicitly described in [6] was obtained by digitizing the points of the scanned grid images. For the convergence of solution, L_2 norms of density variations, $\|\Delta\rho\|$, were reduced to 10^{-5} for all the calculations [9].

In reality, argon and air are injected separately in a segmented arc heater [13]. Air is introduced from the entire wall of the constrictor section and a small amount of argon, for instance 0.03 kg/s in the AHF, is injected from the anode and the cathode. On the other hand, the injection gas was treated as a perfect mixture in ARCFLO4 for simplicity and the mixture injection was distributed uniformly over the side wall of the constrictor as shown in Fig. 2. The wall temperature was fixed at 1100 K and the wall density was determined by the equilibrium relation between the wall temperature and pressure [4]. The outlet condition was extrapolated from the value of the inner computational domain because the region after the nozzle throat was supersonic.

B. Equilibrium Composition

In the previous works [9–11], it was assumed that the working gas mostly consisted of air. However, a small amount of argon is injected from the electrodes to ensure that sufficient ionization is maintained near the surface of the electrodes. Thus, realistic working gas should be an air–argon mixture. To obtain the thermodynamic and transport properties of the working gas, equilibrium composition of the species is essential.

Chemical equilibrium is usually described by either of the two equivalent formulations, equilibrium constant or minimization of free energy. In this study, the minimization of free energy

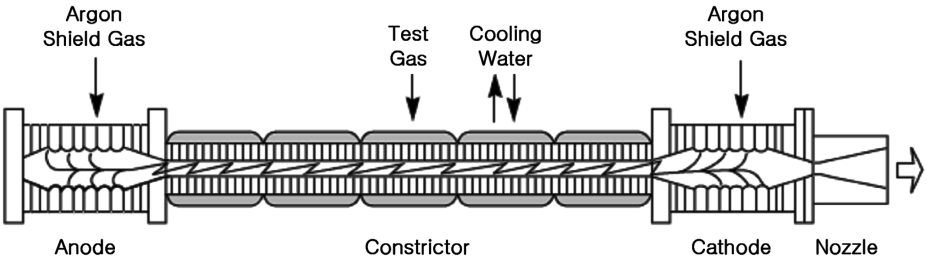

Fig. 1 A schematic drawing of a segmented arc heater.

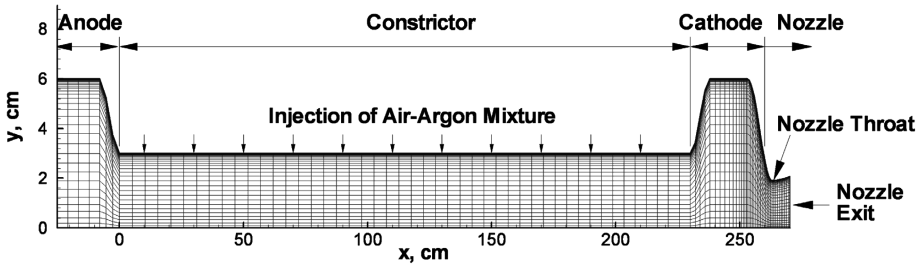

Fig. 2 Grid system of the Aerodynamic Heating Facility arc heater (96 × 50 mesh).

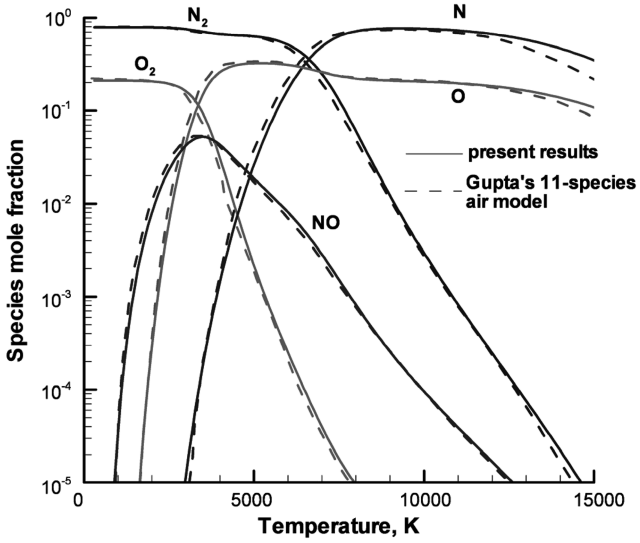

a) Neutral species

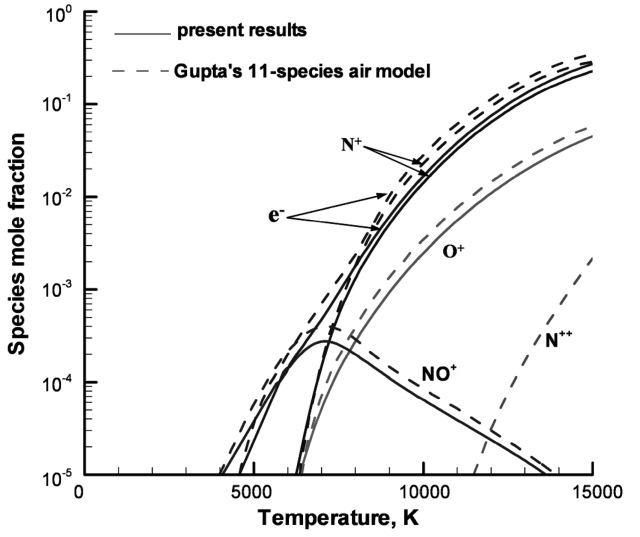

b) Charged species

Fig. 3 Equilibrium composition of air ($p = 1$ atm).

formulation [16] was used because each species can be treated independently without specifying a set of reactions a priori.

Before obtaining the thermodynamic and transport properties of the air–argon mixture, equilibrium composition of air was computed and then compared with the data of [17] to verify the accuracy of the computed results. The present equilibrium composition was obtained with a 9-species air model (N_2, O_2, N, O, NO, N^+, O^+, NO^+, and e^-), whereas the result of [17] was based on an 11-species air model (N_2, O_2, N, O, NO, N^+, O^+, NO^+, N^{++}, O^{++}, and e^-). As shown in Fig. 3, the present 9-species air model yields species mole fractions very similar to that obtained from the 11-species air model. It is known that the small concentrations of N^{++} and O^{++} do not affect the equilibrium thermodynamic properties significantly for the temperature range less than 15,000 K.

C. Thermodynamic Properties

Using the composition data obtained by the Gibbs free energy minimization, density, enthalpy, and specific heat of the mixture are directly calculated by

$$\rho = \frac{p}{RT}\frac{\sum_{j=1}^{N_S} n_j M_j}{\sum_{j=1}^{N_S} n_j} \tag{1}$$

$$h = \frac{\sum_{j=1}^{N_S} n_j H_j^\circ}{\sum_{j=1}^{N_S} n_j} \tag{2}$$

$$C_p = \left.\frac{\partial h}{\partial T}\right|_{p=\text{const}} \tag{3}$$

where N_S is the total number of chemical species. M_j and n_j are the molecular weight and number density of species j, respectively. Also, H_j°, which is the standard-state molar enthalpy for specific j at temperature T, is defined as follows:

$$H_j^\circ = H_c + a_1(T - T_s) + \frac{a_2}{2}\left(T^2 - T_s^2\right) + a_3\left(\frac{1}{T} - \frac{1}{T_s}\right) \tag{4}$$

where T_s is called the split temperature, 3000 K. Also, H_c, a_1, a_2, and a_3 can be obtained from the Joint Army–Navy–Air Force (JANAF) thermodynamic data [18].

Before obtaining the thermodynamic properties for the air–argon mixture, thermodynamic properties of air were computed for pressures of 1 and 10 atm to compare with the data of [19], which were based on the curve fit model obtained from the 11-species air model. As shown in Fig. 4, the present 9-species air model provides thermodynamic properties very similar to those obtained from the 11-species air model of [19] for temperatures up to about 12,000 K. In this study, the temperature of interest seldom exceeded 12,000 K.

D. Transport Properties

To calculate transport properties such as viscosity, electrical conductivity, and thermal conductivity, the approximate formulations of [20,21] were used instead of the complete kinetic theory expressions in [22]. They require the data on the collision integral, which is classified into the momentum transfer cross section $\pi\Omega_{ij}^{(1,1)}$ and the viscosity cross section $\pi\Omega_{ij}^{(2,2)}$, between all the couples of species in arc-heater flows. In this study, most collision cross sections including the air species were obtained from [23,24]. However, for the ionized species, the effective Coulomb cross section [20,21] was used and the formulas are as follows:

$$\pi\Omega_{ee}^{(2,2)} = 1.29 Q_c \times 10^{16} \qquad \text{(for electrons)} \tag{5}$$

$$\pi\Omega_{II}^{(2,2)} = 1.36 Z^4 Q_c \times 10^{16} \qquad \text{(for ions)} \tag{6}$$

$$\pi\Omega_{ee}^{(1,1)} = \pi\Omega_{II}^{(1,1)} = 0.795 Z^4 Q_c \times 10^{16} \quad \text{(for electrons and ions)} \tag{7}$$

where $Z = 1$ for single ionized species and

$$Q_c = \frac{e^4}{(kT)^2}\ell_n \Lambda \tag{8}$$

The shielding parameter Λ is defined as

$$\Lambda = \left[\frac{9(kT)^3}{4\pi e^6 n_e} + \frac{16(kT)^2}{e^4 n_e^{2/3}}\right]^{1/2} = \left[2.09 \times 10^{-2}\left(\frac{T^4}{10^{12} p_e}\right) + 1.52\left(\frac{T^4}{10^{12} p_e}\right)^{2/3}\right]^{1/2} \tag{9}$$

where T is the temperature in Kelvin, $p_e = n_e kT$ is the electron pressure in atmosphere, and $e = 4.8 \times 10^{-10}$ esu (electrostatic unit of charge) is the electron charge.

By using the data on the compositions and the collision integrals, transport properties can be calculated.

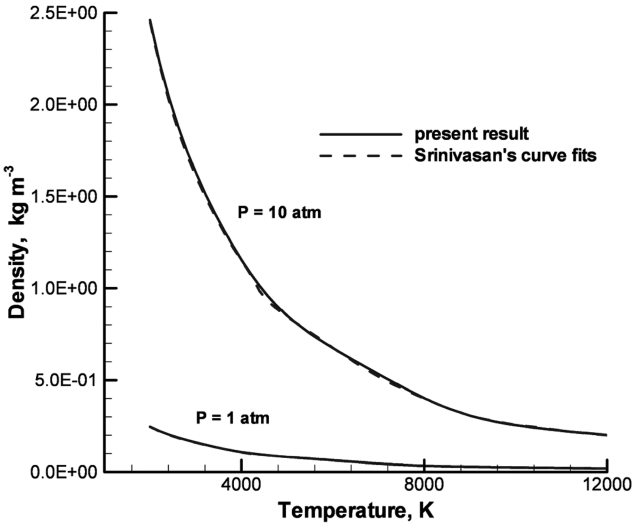

a) Density

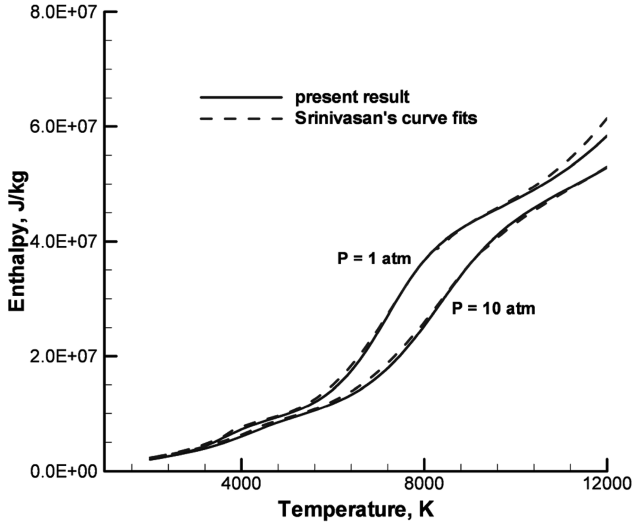

b) Enthalpy

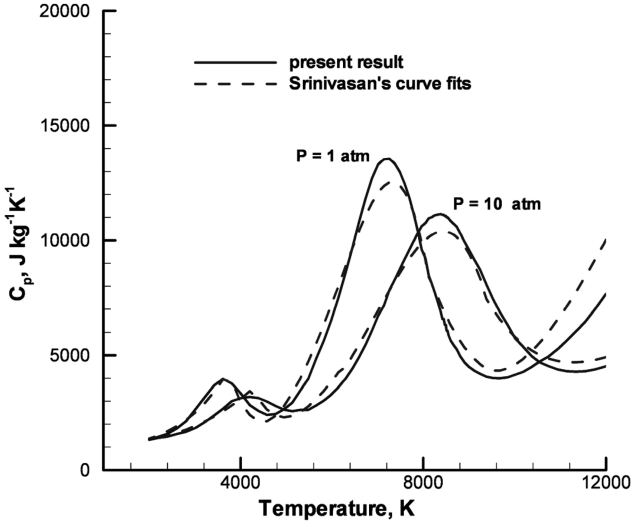

c) Specific heat

Fig. 4 Comparison of thermodynamic properties.

1) Viscosity:

$$\mu = \sum_{i=1}^{N_S} \left(\frac{\frac{M_i}{N_A} n_i}{\sum_{j=1}^{N_S} n_j \Delta_{ij}^{(2)}} \right) \tag{10}$$

2) Electrical conductivity:

$$\sigma = \frac{e^2}{kT} \frac{n_e}{\sum_{j=1, j\neq e}^{N_S} n_j \Delta_{ij}^{(1)}} \tag{11}$$

3) Thermal conductivity:

$$\kappa = \kappa_{\text{tr}} + \kappa_{\text{int}} + \kappa_{\text{re}} \tag{12}$$

where the translational thermal conductivity is

$$\kappa_{\text{tr}} = \frac{15}{4} k \sum_{i=1}^{N_S} \left(\frac{n_i}{\sum_{j=1}^{N_S} a_{ij} n_j \Delta_{ij}^{(2)}} \right) \tag{13}$$

and the internal thermal conductivity is

$$\kappa_{\text{int}} = k \sum_{i=1}^{N_S} \left(\frac{[\frac{C_{p,i}}{R} - \frac{5}{2}] n_i}{\sum_{j=1}^{N_S} n_j \Delta_{ij}^{(1)}} \right) \tag{14}$$

and the reaction thermal conductivity is

$$\kappa_{\text{re}} = k \sum_{l=1}^{N_{\text{IR}}} \frac{(\frac{\Delta h_l}{RT})^2}{\sum_{l=1}^{N_S} \frac{a_{l,i}}{x_i} \sum_{j=1}^{N_S} (a_{l,i} n_j - a_{l,j} n_i) \Delta_{ij}^{(1)}} \tag{15}$$

N_{IR} is the total number of independent reactions in the system and $a_{l,i}$ represents the stoichiometric coefficient of the component A_i in the lth chemical reaction written in the balance form:

$$\sum_{i=0}^{N_S} a_{l,i} A_i = 0 \tag{16}$$

In the previous equations,

$$\Delta_{ij}^{(1)} = \frac{8}{3} \left[\frac{2 M_i M_j}{\pi RT (M_i + M_j)} \right]^{1/2} \pi \Omega_{ij}^{(1,1)} \tag{17}$$

$$\Delta_{ij}^{(2)} = \frac{16}{5} \left[\frac{2 M_i M_j}{\pi RT (M_i + M_j)} \right]^{1/2} \pi \Omega_{ij}^{(2,2)} \tag{18}$$

$$\alpha_{ij} = 1 + \frac{[1 - \frac{M_i}{M_j}][0.45 - 2.54 \frac{M_i}{M_j}]}{[1 + (\frac{M_i}{M_j})]^2} \tag{19}$$

To verify the accuracy of the calculation, the transport properties of the air were compared with the data of several references. In Fig. 5a, the present calculated viscosity is compared with the calculation of Gupta et al. [17], Murphy [25], Bacri and Raffanel [26], Elchinger et al. [27], and Yos [21]. The present result is similar to Gupta et al.'s because the same kinetic equation was used. Figure 5b shows the thermal conductivity. The present calculated thermal conductivity was compared with the experimental values of Devoto et al. [28] and Asinovsky et al. [29], and the calculations of Gupta et al. [17], Murphy [25], Bacri and Raffanel [26], Elchinger et al. [27], and Yos [21]. The present result agreed reasonably with the experimental data at temperatures up to 8000 K and was similar to Gupta et al.'s. The thermal conductivity insignificantly affects the arc-heater flows because most heat energy is transferred by radiation and turbulent mixing. In Fig. 5c, electrical conductivity, one of the important parameters for calculating Joule heating in the arc-heater flows, is shown. In the figure, the present result is compared with the experimental values of Asinovsky et al. [29] and Schreiber et al. [30], calculations of Murphy [25] and Capitelli et al. [31], and results of

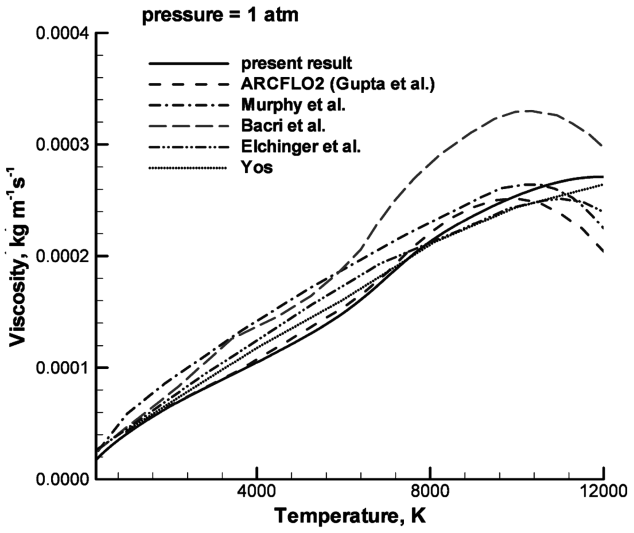

a) Viscosity

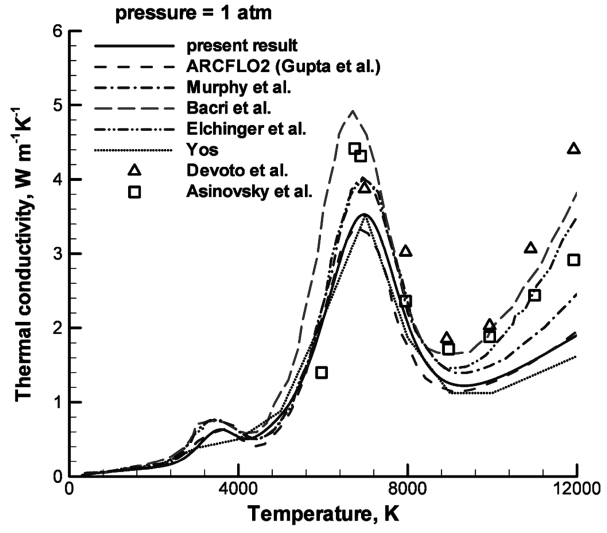

b) Thermal conductivity

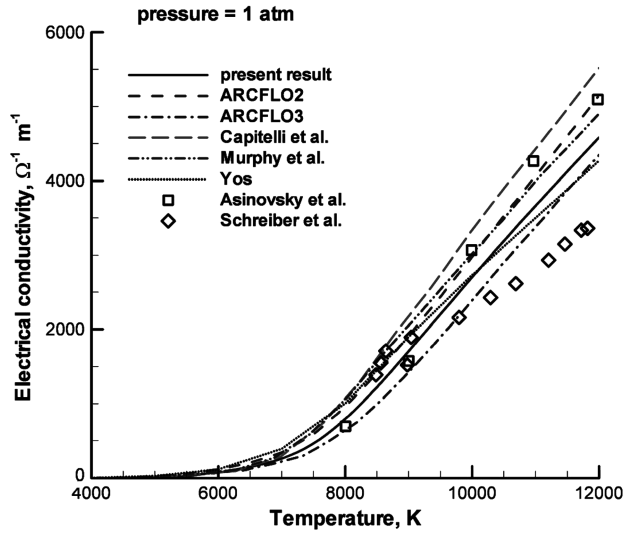

c) Electrical conductivity

Fig. 5 Comparison of transport properties.

ARCFLO2 and ARCFLO3. The difference between the various calculations was due to the selection of the collision integral for the different species and due to the different kinetic equations used for calculating electrical conductivity.

E. Joule Heating Modeling

Ideally, the Joule heating by arc should be obtained by solving the Maxwell equations. However, if the current distribution is known, it can be simply calculated by Ohm's law. Because the constrictor wall was insulated electrically, the current in the constrictor was constant. Under the assumption that the voltage gradient was independent of the radius of the constrictor, the Joule heating can be simplified as follows.

Ohm's law for a cylindrical column is

$$j(x, y) = \sigma(x, y) \cdot E(x) \tag{20}$$

$$E(x) = \frac{j(x, y)}{\sigma(x, y)} = \frac{\int_0^R 2\pi y j(x, y)\,\mathrm{d}y}{\int_0^R 2\pi y \sigma(x, y)\,\mathrm{d}y} = \frac{I}{\int_0^R 2\pi y \sigma(x, y)\,\mathrm{d}y} \tag{21}$$

where

$$I = \int_0^R 2\pi y j(x, y)\,\mathrm{d}y = \text{const} \tag{22}$$

from Kirchhoff's law of the conservation of current.

Finally, the Joule heating is given by

$$j(x, y) \cdot E(x) = \frac{I^2 \sigma(x, y)}{[\int_0^R 2\pi y \sigma(x, y)\,\mathrm{d}y]^2} \tag{23}$$

Figure 6 shows the current distribution along the axial direction.

F. Radiation Modeling

For high temperature flow, radiation is an important heat transfer mode together with thermal convection. The radiative heat flux is calculated by the radiative transfer equation of Eq. (24):

$$-\frac{1}{\rho \kappa_\nu}\frac{\mathrm{d}I_\nu}{\mathrm{d}s} = I_\nu - B_\nu \tag{24}$$

where I_ν is the radiative intensity along the ray, s. The absorption coefficient κ_ν, which was obtained from experiment, is a function of frequency, temperature, and pressure. The Planck function B_ν is written as follows:

$$B_\nu = \frac{2h}{c^2}\frac{\nu^3}{e^{h\nu/kT} - 1} \tag{25}$$

When the radiative intensity at a given point is calculated for all directions, the radiant flux per unit frequency expressed in cylindrical

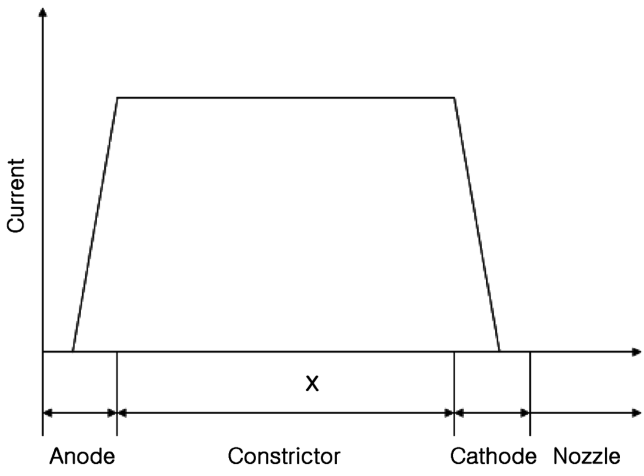

Fig. 6 The current distribution in the arc heater.

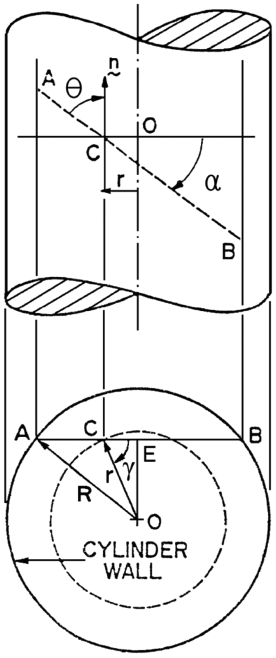

Fig. 7 A cylindrical geometry and coordinate system.

coordinates can be calculated as (see Fig. 7)

$$q_\nu(r) = \int_\Omega I_\nu(r)\cos\theta\,\mathrm{d}\Omega \tag{26}$$

The details can be found in [1]. Then the total radiant flux, integrated over all frequencies, is calculated as

$$q_R(r) = \int_0^\infty q_\nu(r)\,\mathrm{d}\nu \tag{27}$$

In a discrete form, Eq. (27) becomes

$$q_R(r) = \sum_n q_n(r) \tag{28}$$

To obtain accurate radiation, the line-by-line calculation [32] is the most desirable method. However, the computation cost for such a calculation is formidable. Thus, Sakai et al. developed a new three-band model that can compute radiative transport equations 400 times faster than the detailed line-by-line calculation without compromising accuracy [6]. In this model, three absorption coefficients, defined at a given wavelength, are functions of pressure and temperature over the pressure range of 1–10 atm and the temperature range of 1000–15,000 K. In the present study, we adopted the three-band radiation model [6] to describe the radiative flow physics in the arc heaters accurately. Concerning the influence of argon atoms on a radiative flux, argon atoms are counted as air atoms because the radiation power emitted by argon is similar to that from oxygen and nitrogen atoms at the same enthalpy [33].

G. Turbulence Modeling

Turbulence is regarded as one of the key phenomena in arc-heater flows [9]. For its modeling, algebraic turbulence models have been widely used wherein the turbulent fluctuating quantities are correlated to the mean flow quantities by algebraic relations. In the previous studies [9–11], we tested k–ε [12], k–ω [34], and k–ω shear stress transport (SST) [35] two-equation turbulence models which can express the convective flow physics of turbulence and do not explicitly demand the mixing length. And it was observed that the k–ε turbulence model combined with the three-band radiation model was the most appropriate in analyzing arc-heater flows. Also, it was shown that the influence of turbulence on the heat transfer mechanism is as much as or bigger than that of radiation. It was confirmed that an accurate turbulence model is one of the key requisites for a reliable prediction of arc-heater performance [9]. In accordance with [9], we adopted the k–ε turbulence model for the description of the turbulent flow physics in arc heaters.

III. Results

Computations for AHF at the NASA Ames Research Center were carried out. The AHF is operated with a 20 MW constricted arc heater which produces a pressure range of 1–9 atm and an enthalpy level of 1–33 MJ/kg. Recently, Hightower et al. [36] carried out a series of arc-jet tests in the AHF using the energy balance method. Sakai and Olejniczak [6] computed those flows using ARCFLO3 and compared the results with Hightower's experimental data.

A. Comparison of Operational Data

In the present study, computational and experimental results were compared for the AHF arc heater in a similar manner to Sakai's study. The basic operational data such as the voltage between electrodes, the mass-averaged enthalpy at the nozzle throat, pressure in the cathode chamber, and the arc-heater efficiency were compared with the experimental data. The mass-averaged enthalpy and efficiency are defined as follows.

Mass-averaged enthalpy (J/kg):

$$H_a(x) = \frac{\int_0^R 2\pi y\rho(x,y)u(x,y)H(x,y)\,\mathrm{d}y}{\int_0^R 2\pi y\rho(x,y)u(x,y)\,\mathrm{d}y} \tag{29}$$

Efficiency (%):

$$\eta = \frac{\text{power absorbed by flow}}{\text{power input}} = 100\times\left(1-\frac{q_R - q_c}{I\cdot V}\right) \tag{30}$$

In the previous studies [9–11], the working gas was air. And, its thermodynamic and transport properties were calculated by using the curve fitted data [17,19] which are widely used because of their convenience. However, in the present study, thermodynamic and transport properties were obtained by the new procedure. To validate the present procedure, the airflow in the AHF arc heater was calculated for $I = 1600$ A. As shown in Figs. 8, most of the computed data agree well with the experimental data except for pressure. In Fig. 8c, although the computed pressure agrees well with the experimental data at a high mass flow rate, the difference between the experimental data and the computation becomes larger as the mass flow rate decreases. It reaches about 35% at the mass flow rate of 0.07 kg/s. We conjecture that the uncertainty of experimental data mainly accounts for the large difference at the low mass flow rate. Physically, as the mass flow rate approaches zero, the pressure in the constrictor should also approach zero. However, in Fig. 8c, the experimental data approach about −0.23 atm while the computed pressure approaches zero. Because the pressure slops of experimental data and computational results are similar to each other, it is reasonable to consider the shift-down effect in the experimental data. Then, the difference between experiment and simulation reduces to 10% at the mass flow rate of 0.07 kg/s. When compared with the previous curve fit model, the present model shows similar results to the previous curve fit model except for the voltage plot. The difference between calculated voltages originates from the model of electrical conductivity because there is little difference between thermodynamic properties and transport properties except the electrical conductivity.

Actually, the working gas is an air–argon mixture. The mass flow rate of argon injected in the anode and cathode is 0.015 kg/s, respectively. The present study simply considered these gases as air mixtures including argon of 0.03 kg/s in the same way as in Sakai's study. Table 1 shows the ratio of argon to the mixture for AHF. Figure 9 shows the comparison between the present mixture case and previous air case. In Fig. 9a, the computed voltage agrees very well with the experimental data. They approach closer to the experimental data as the ratio of argon increases. In Fig. 9b, the computed mass-averaged enthalpy shows a different trend from the previous air case

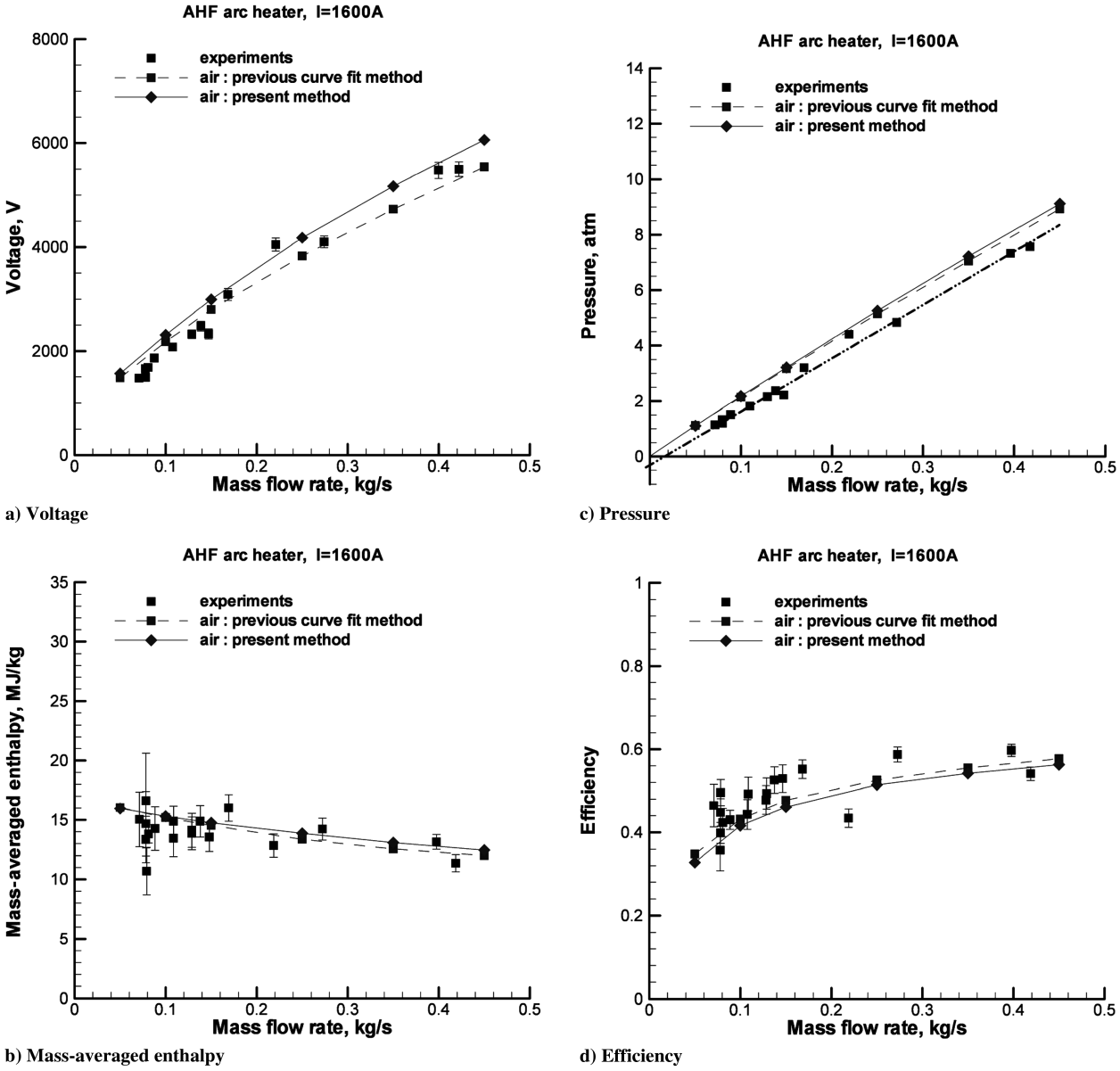

Fig. 8 Comparison between air models.

at low mass flow rate and follows the tendency of Sakai's results which considered argon effects. In Fig. 9c, the computed pressure agrees well with the experimental data. In Fig. 9d, the computed efficiency is predicted fairly well at low mass flow rate but seems to somewhat deviate from the experimental data compared with the air case.

Based on the results in Fig. 9, however, we cannot say for certain that the accuracy of the computation is always improved with the consideration of argon gas. The reason seems to originate from the excessive consideration of the argon effect. In reality, the argon gas injected from the cathode may have little influence on the flow in the constrictor. The ratio of argon in the constrictor is mainly determined by the amount of argon from the anode. Thus, it is more reasonable to consider the argon gas, about 0.015 kg/s in the AHF, injected from the anode only. Table 2 shows the ratio of the argon injected from the anode only to the mixture, and Fig. 10 shows the results for this case. The voltage agrees very well with the experimental data. Especially, the behavior of the mass-averaged enthalpy is remarkable. It agrees very well with experiment. Pressure also agrees well with the experimental data and is less dependent on chemical composition. Efficiency is improved although some deviation from the experimental data is still observed.

Table 1 Ratio of argon injected from electrodes to mixture

Mass flow rate of working gases	Ratio of argon to mixture
0.05 kg/s	60%
0.10 kg/s	30%
0.15 kg/s	20%
0.25 kg/s	12%
0.35 kg/s	8.57%
0.45 kg/s	6.67%

B. Argon Effect: Calculation with Fixed Current

Operational experience of the arc heater has shown that argon injected into the electrodes reduces electrode wear and contributes to the prevention of arcing between the constrictor disks and electrode rings. Thus, a small amount of argon is always injected in the anode and cathode. To understand the arc-heater flow physics more accurately, it is essential to investigate the influence of the argon gas on arc-heater flows.

1. Temperature and Specific Heat

Temperature plays an important role in determining the rate and the extent of chemical reactions and it is strongly affected by the

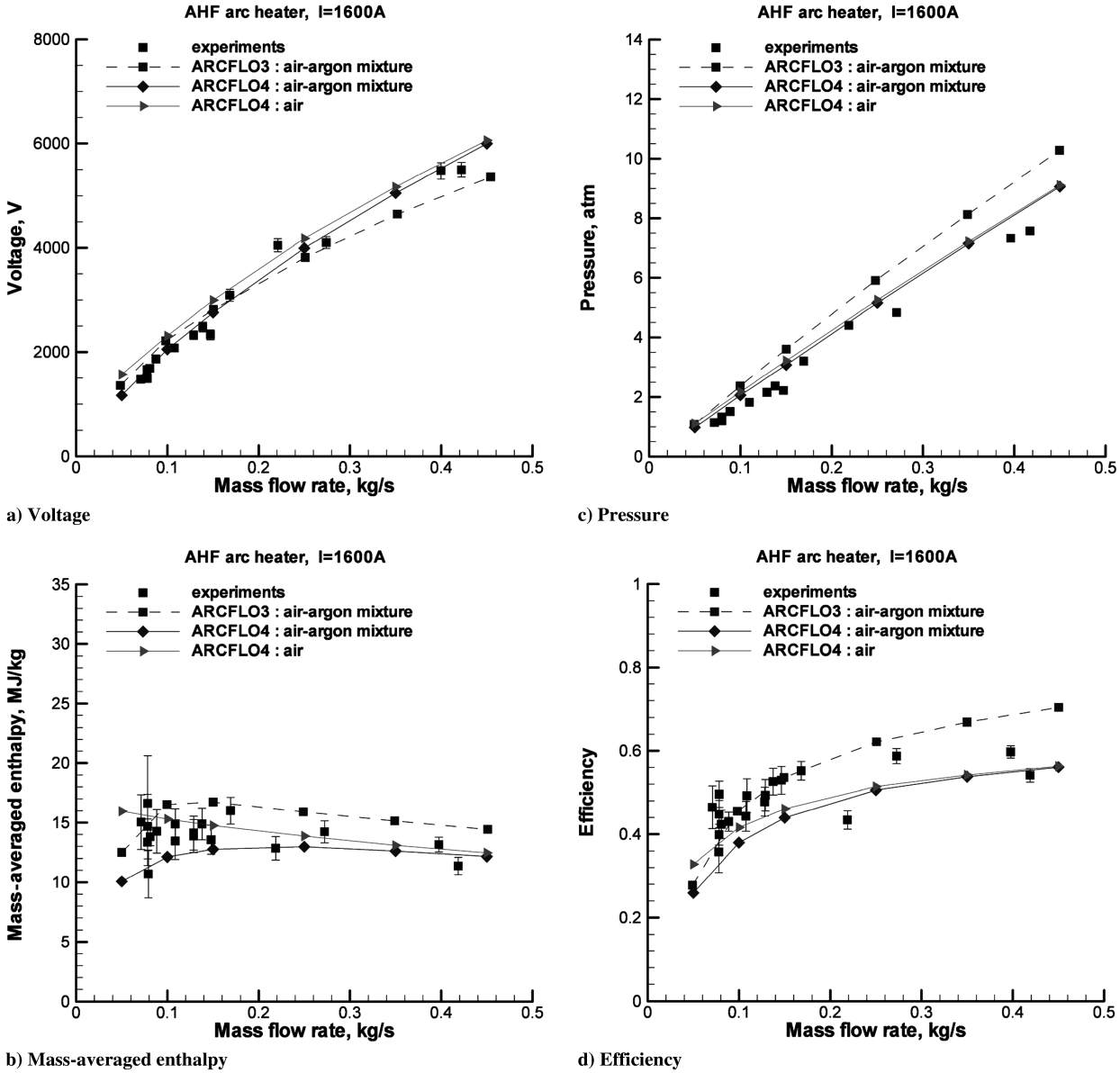

a) Voltage

c) Pressure

b) Mass-averaged enthalpy

d) Efficiency

Fig. 9 Comparison between air and mixture cases.

thermodynamic characteristics of the working gas in an arc heater. Argon, which is one of the working gases, has neither rotational nor vibrational energy because it is a monatomic gas. Also, it does not have chemical energy except for ionization energy, because it is a noble gas which does not react with most other gases. Thus, argon requires smaller heat energy than air to rise to the same temperature. In an arc heater, the temperature of the air–argon mixture can be raised more easily than that of the air with the same Joule heating energy of the arc. Figure 11a shows the specific heat of the air–argon mixture in terms of temperature. In the figure, it is shown that the specific heat of the air–argon mixture is lower than that of the air at the same temperature because of the dissociations of N_2 and O_2 and ionizations of N, O, and Ar. Figure 11b shows the distribution of specific heat along the radial direction at the middle section of the constrictor at the current of 1600 A and the mass flow rate of 0.05 kg/s. It shows that specific heat is low when the argon ratio is high. The three convex curves near the wall surface, in the middle, and at the core are related to the dissociations of O_2 and N_2 and ionizations of N, O, and Ar, respectively. Figure 12 shows the distribution of temperature at the same cross section. The figure shows that temperature becomes higher on the whole and the thickness of the arc column increases as the ratio of argon increases. Also, the temperature distribution around the core becomes flat because of the significant amount of heat energy transferred from the core by the radiation. Figure 13 shows the distribution of the radiant heat flux at the middle cross section of the constrictor. The positive slope of heat flux means heat emission. In the core region, heat emission by radiation is very high and the flow acts like a highly conductive flow from the core to the edge of the arc column. As a result, it makes the temperature distribution flat.

Table 2 Ratio of argon injected from only anode to mixture

Mass flow rate of working gases	Ratio of argon to mixture
0.05 kg/s	30%
0.10 kg/s	15%
0.15 kg/s	10%
0.25 kg/s	6%
0.35 kg/s	4.29%
0.45 kg/s	3.33%

2. *Electron Mole Fraction and Electrical Conductivity*

The electrons in a plasma accelerate more quickly in response to an electric field than the heavier positive ions due to their lower mass, and hence, carry the bulk of the current. Thus, they behave as an

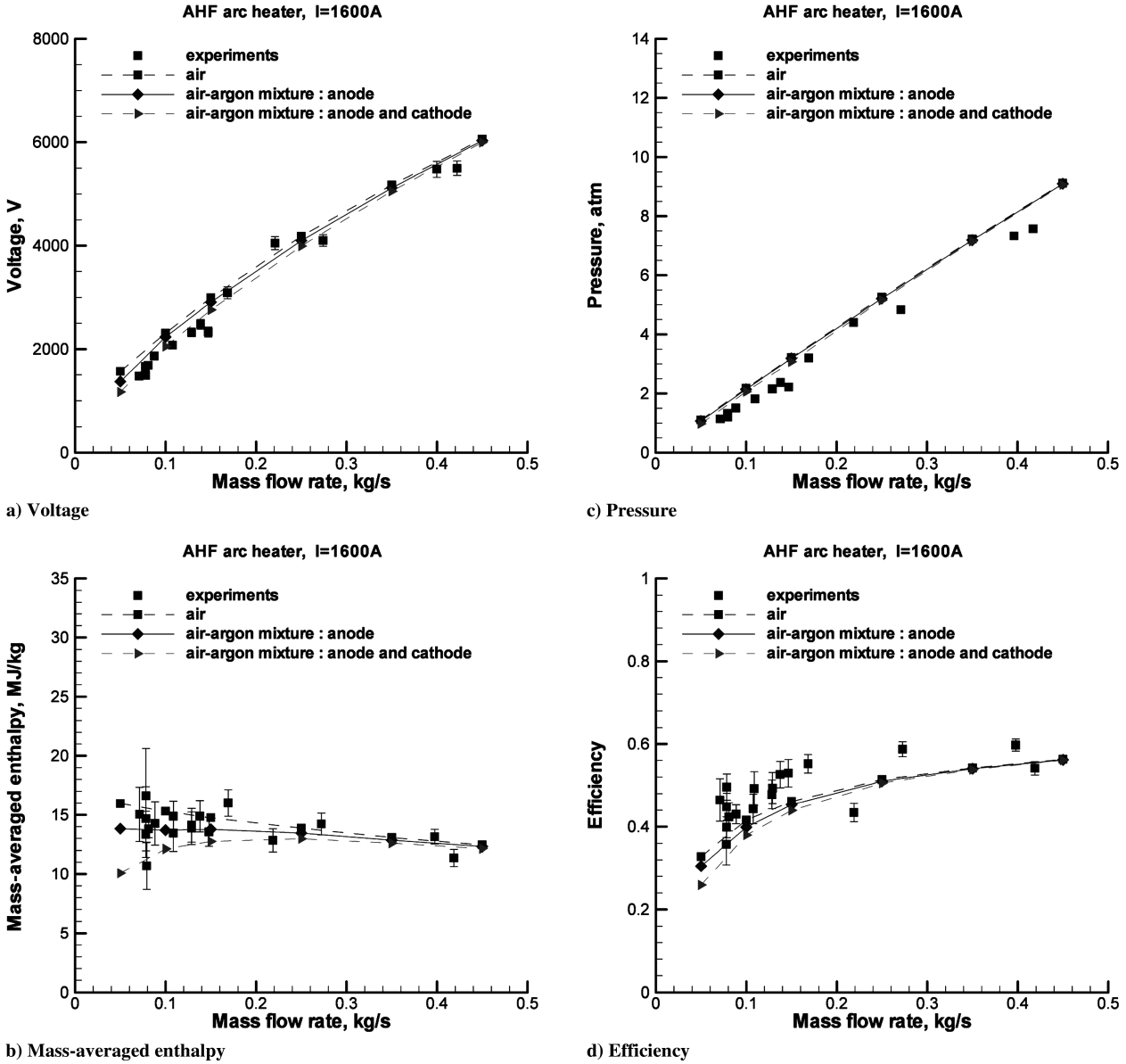

a) Voltage

c) Pressure

b) Mass-averaged enthalpy

d) Efficiency

Fig. 10 Comparison between mixing types.

electrical conductor. The conductivity is highly dependent on the concentration of electrons and is strongly affected by the temperature. Figures 14 and 15 show the distributions of the electron mole fraction and electrical conductivity along the radial direction at the middle section of the constrictor at the current of 1600 A and mass flow rate of 0.05 kg/s, respectively. As the ratio of argon increases, it is shown that the value of electron mole fraction becomes higher and therefore, the electrical conductivity becomes higher on the whole. This, in turn, means that more electrons flow through the working gas and the thickness of the arc column becomes larger. On the other hand, electron mole fraction and electrical conductivity are seen to be slightly lower than those of the air around the core. This is due to the lower ionization rate at the same temperature and the larger molar weight of argon than those of the air.

3. *Voltage Gradient and Joule Heating*

The total amount of Joule heating is the power which is supplied to the arc heater. Generally, Joule heating is closely related to the voltage gradient and electrical conductivity. Figures 15 and 16 show the electrical conductivity and Joule heating at the middle section of the constrictor at a current of 1600 A and mass flow rate of 0.05 kg/s. In Fig. 15, as the ratio of argon increases, the overall value of electrical conductivity becomes higher although the highest value becomes lower, and thus, the magnitude of the voltage gradient becomes lower. It can be said that electrons flow more easily to the cathode. Therefore, Joule heating becomes smaller, as shown in Fig. 16. As a result, the flow enthalpy of the mixture is maintained low.

4. *Arc-Heater Efficiency*

Efficiency of the arc heater is an important factor in predicting flow enthalpy. Figure 17 shows the total Joule heating and total heat energy loss in terms of the ratio of argon. Heat energy loss by thermal conduction decreases according to the decrease of Joule heating as the ratio of argon increases. However, heat energy loss by radiation increases because the arc column becomes thicker and the higher temperature region is located closer to the wall. As a result, the total heat energy loss decreases more slowly than the total Joule heating and the arc-heater efficiency becomes relatively lower as the ratio of argon increases. Figure 18 shows this phenomenon more clearly. Figure 18a shows the distributions of Joule heating and total heat energy loss along the axial direction. The heat energy obtained from Joule heating decreases more than the total energy loss as the ratio of argon increases. Figure 18b shows that the heat energy loss by thermal conduction decreases, whereas the heat energy loss by radiation increases as the ratio of argon increases.

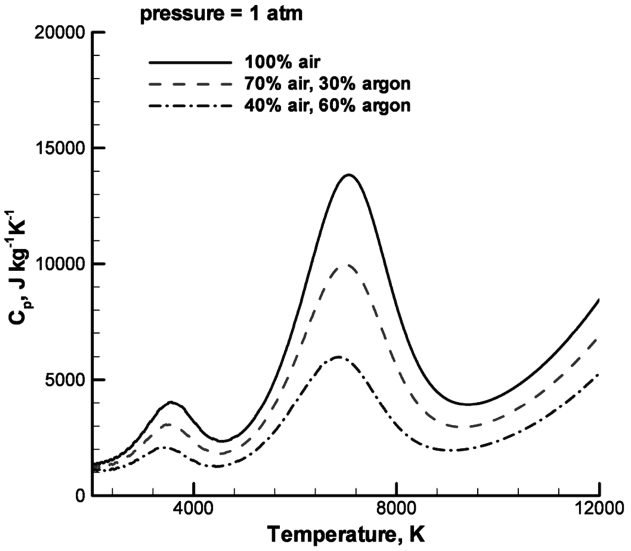

a) Specific heat of air-argon mixture

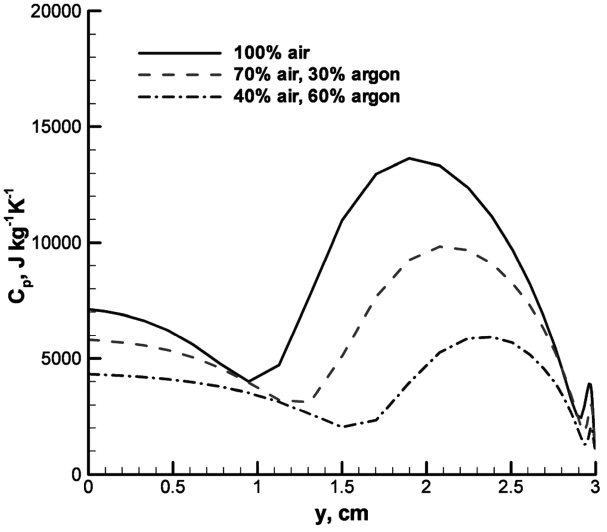

b) Specific heat distribution in constrictor

Fig. 11 Specific heat of air–argon mixture.

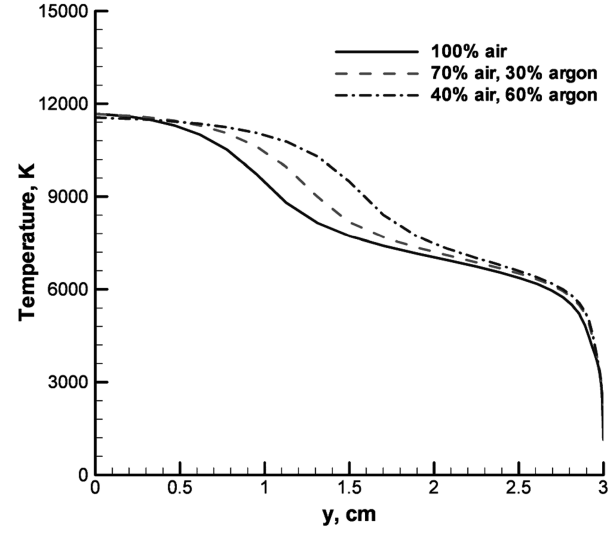

Fig. 12 Temperature distribution at the middle of the constrictor.

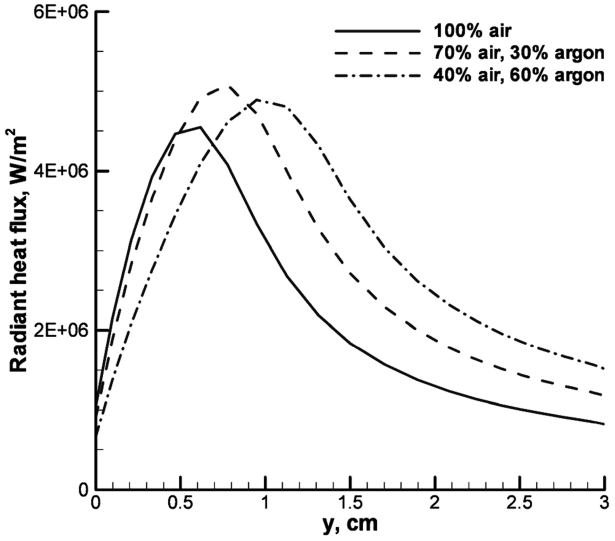

Fig. 13 Radiant heat flux distribution at the middle of the constrictor.

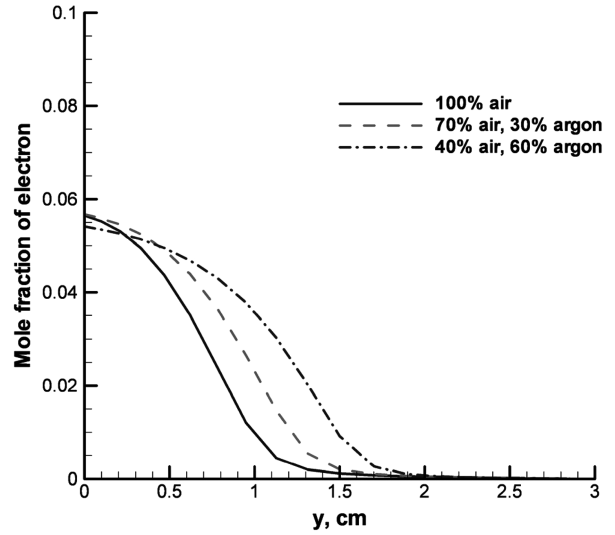

Fig. 14 Electron mole fraction distribution at the middle of the constrictor.

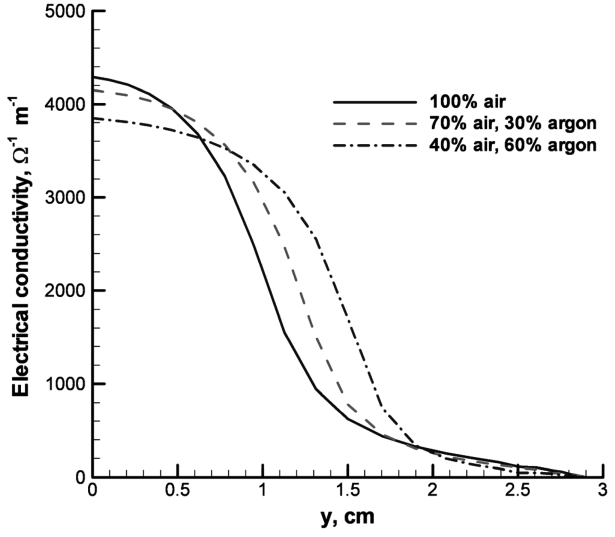

Fig. 15 Electrical conductivity distribution at the middle of the constrictor.

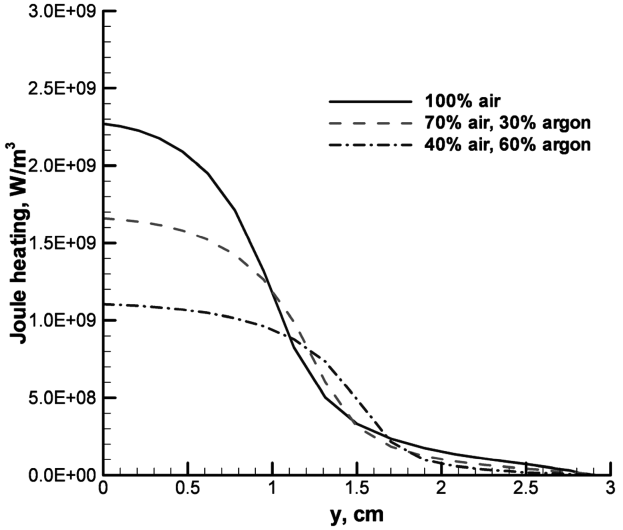

Fig. 16 Joule heating distribution at the middle of the constrictor.

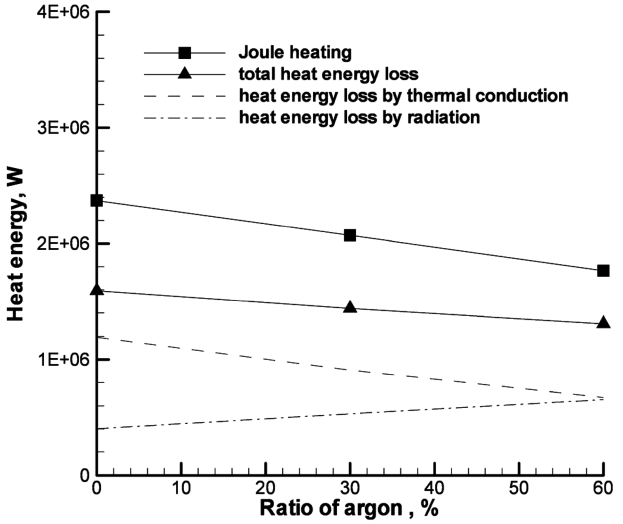

Fig. 17 Total Joule heating and heat energy loss.

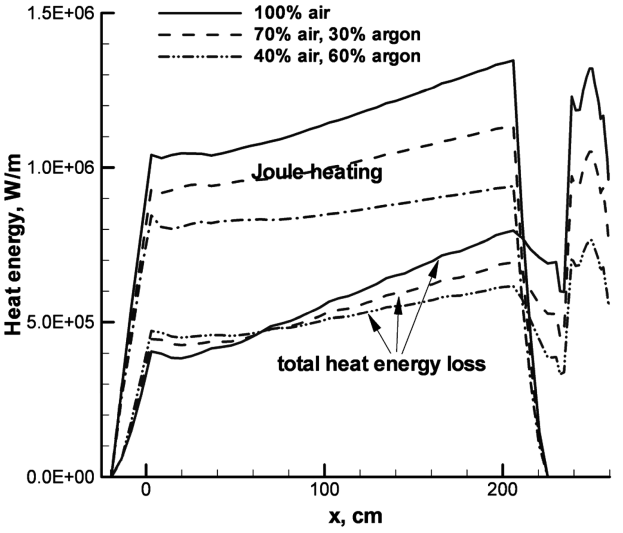

a) Comparison between Joule heating and total heat energy loss

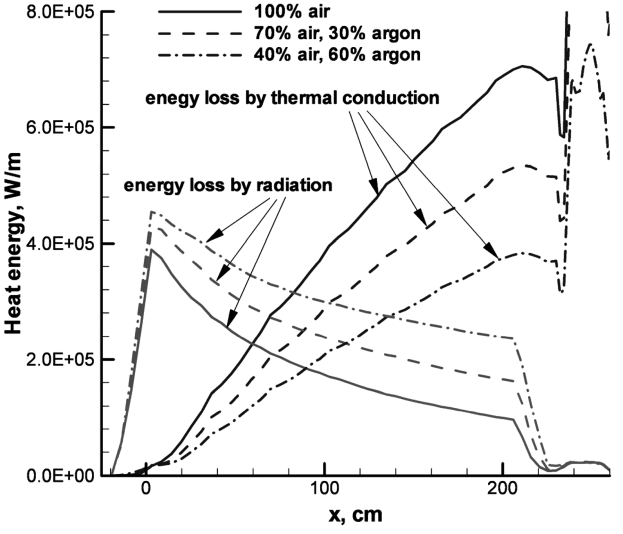

b) Comparison of energy loss between thermal conduction and radiation

Fig. 18 Joule heating and heat energy loss along axial direction.

5. Enthalpy

Enthalpy is one of the most important parameters as well as the total pressure in the ground test. From the results of Joule heating and efficiency, it can be deduced that the flow enthalpy decreases as the ratio of argon increases. Figure 19 shows the distribution of the total enthalpy along the radial direction at the middle section of the constrictor at a current of 1600 A and a mass flow rate of 0.05 kg/s. In the figure, it is confirmed that the total enthalpy decreases as the ratio of argon to the air–argon mixture increases. In the viewpoint of the ratio of centerline enthalpy to mass-averaged enthalpy, the ratio becomes lower and closer to unity. From the distribution of the enthalpy, the flat region around the core is wider, that is, the thickness of the arc column is larger as the ratio of argon increases. As a result, the difference between centerline enthalpy and mass-averaged enthalpy is reduced and the ratio is between 1.08 and 1.12. Concerning this issue, Sakai insisted that the ratio varied from 1.3 to 1.5 using the ARCFLO3 code [8]. A sharp difference between ARCFLO4 and ARCFL3 is the turbulence model. ARCFLO3 adopts an algebraic turbulence model, whereas ARCFLO4 adopts a two-equation turbulence model. The two-equation turbulence model produces stronger turbulent flow in the core region. Thus the heat energy transfer toward the wall becomes larger and the centerline-to-average enthalpy ratio becomes lower [9]. So far, it is not clear which is right, ARCFLO3 or ARCFLO4, because both of the computed

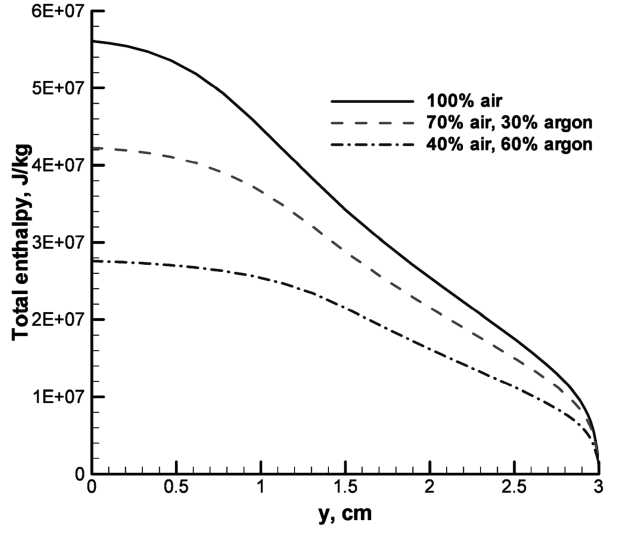

Fig. 19 Total enthalpy distribution at the middle of the constrictor.

Table 3 Operational data

Operational data	100% air		70% air 30% argon	40% air 60% argon	
	Fixed power	Fixed current		Fixed power	Fixed current
Current	1365 A	1600 A	1600 A	1900 A	1600 A
Voltage	1618 V	1578 V	1373 V	1157 V	1172 V
Power	2.195 MW	2.525 MW	2.197 MW	2.198 MW	1.876 MW
Mass-averaged enthalpy	15.06 MJ/kg	15.97 MJ/kg	13.83 MJ/kg	9.99 MJ/kg	10.07 MJ/kg
Chamber pressure	1.068 atm	1.104 atm	1.066 atm	0.942 atm	0.978 atm
Heater efficiency	34.73%	32.82%	30.53%	23.09%	25.92%

results were within the error bar of the experimental data. Therefore, it is necessary to study the centerline-to-average enthalpy ratio in detail. Roughly, we may consider the two points for the accurate prediction of the centerline-to-average enthalpy ratio. One is that thermodynamic and transport models should be improved at high temperatures over 10,000 K. Especially, the conductivity of the present code should be improved. It is somewhat different from the experimental data and other models at high temperature over 10,000 K (see Fig. 5). The other is that the turbulent flow at high temperature should be improved because the viscosity is so high at high temperatures that the transition to turbulent flow is delayed. However, the standard k–ε model cannot consider the influence of high temperature.

C. Argon Effect: Calculation with Fixed Input Power

In the previous section, when the input current is fixed for the comparison with experimental data, the power decreases as the ratio of argon increases (see Table 3). Thus, the flow enthalpy decreases due to the lower power as well as higher radiation energy loss. For a more simplified comparison, we calculated the fixed input power cases. Figures 20–24 show the distributions of thermodynamic and electrical properties along the radial direction at the middle section of the constrictor. All present tendencies are similar to the cases where the current is fixed. Each tendency becomes more evident than the fixed current cases. Comparing the cases in which the ratio of argon is 60%, the temperature around the core is higher and the thickness of the arc column is larger according to the increase of the current. Also, the electron mole fraction, electrical conductivity, and Joule heating are higher. However, voltages are seen to be similar among the cases although the current is much different as shown in Fig. 25. It can be deduced that if a current is increased to supply more power to a flow, most of the additional energy contributes to the ionization of the flow at the edge of the arc column and to the increase of the mole fraction of the electrons for balancing the increased current.

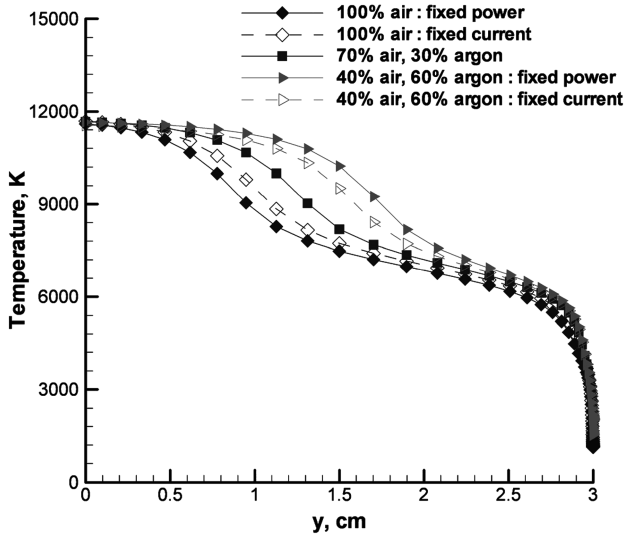

Fig. 20 Temperature distribution at the middle of the constrictor.

Figure 26 shows the efficiency in terms of the argon ratio. The efficiency is reduced as the power and the ratio of argon increase, that is, as the arc column becomes thicker and the heat energy loss by the radiation increases. The thickness of the arc column is one of the important factors for predicting efficiency, which is finally used to predict the mass-averaged enthalpy. In addition, the thickness of the arc column directly influences the ratio of the centerline enthalpy to the mass-averaged enthalpy. In the present study, the effect of argon gas on the thickness of the arc column was observed. However, there

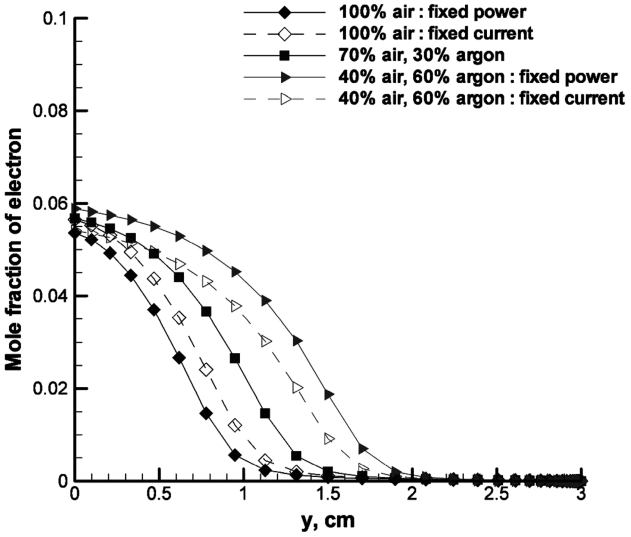

Fig. 21 Electron mole fraction distribution at the middle of the constrictor.

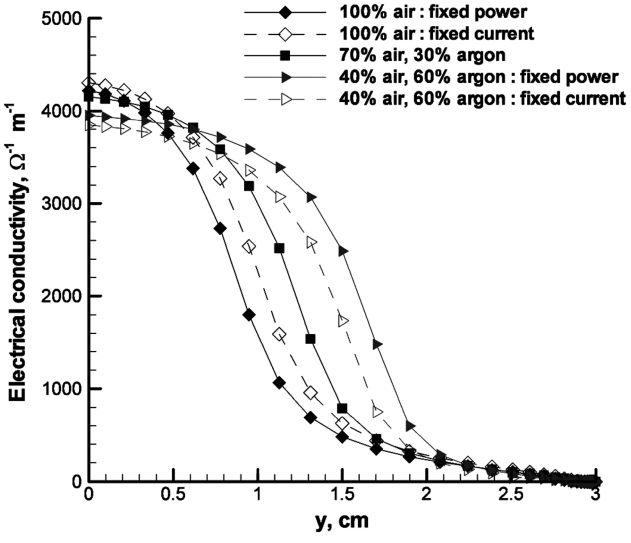

Fig. 22 Electrical conductivity distribution at the middle of the constrictor.

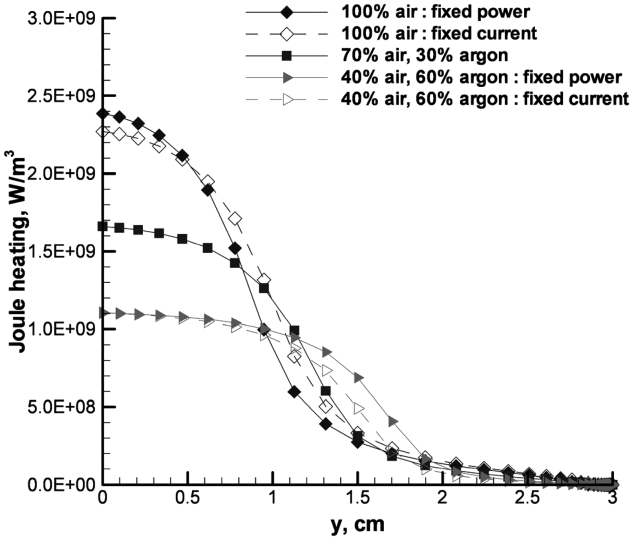

Fig. 23 Joule heating distribution at the middle of the constrictor.

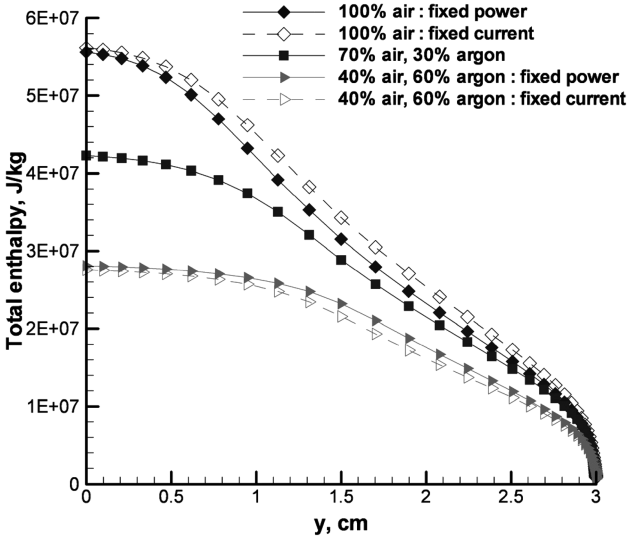

Fig. 24 Total enthalpy distribution at the middle of the constrictor.

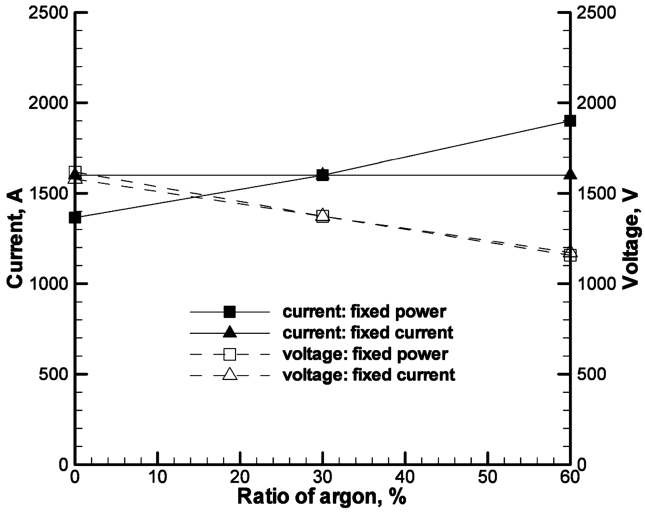

Fig. 25 Voltage and current.

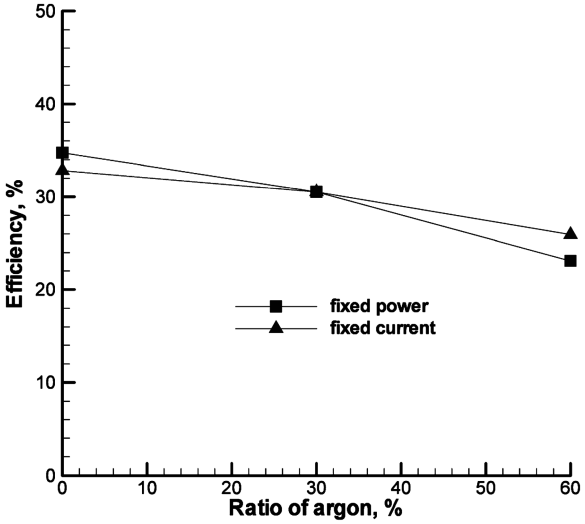

Fig. 26 Efficiency.

is another important factor that determines the thickness of the arc column. In reality, the electromagnetic force is generated when the current flows along the constrictor and it plays a role in the decrease of the thickness of the arc column. Therefore, it seems that the arc column was predicted a little thicker than real physics in the present calculation and efficiency became lower accordingly. For more accurate predictions of efficiency and the ratio of centerline enthalpy to mass-averaged enthalpy, the electromagnetic force should be considered and our future work will consider this effect.

IV. Conclusions

The ARCFLO4 code was improved to simulate the air–argon mixture flows. The thermodynamic and transport properties of the air–argon mixture were calculated under the assumption of a thermal equilibrium condition. The equilibrium composition was calculated by the minimization of the Gibbs' free energy. The thermodynamic properties were obtained directly from the equilibrium composition and species thermochemical properties. The calculation of the transport properties was based on the approximation of the Chapman–Enskog formula. The calculated thermodynamic and transport properties were used to investigate the effect of the argon gas on the arc-heater flows. With the present code, the flow analysis of the 20-MW Aerodynamic Heating Facility at the NASA Ames Research Center was conducted. Through comparisons between the air model and the air–argon mixture model, it was observed that the thermodynamic and electrical characteristics of argon affect the arc-heater flows strongly at low mass flow rates, and thus, its effects should be taken into account. Also, it was confirmed that as the ratio of argon increased, the specific heat became lower, the thickness of the arc column became larger, and electrons flowed more easily accordingly. In addition, the arc-heater efficiency decreased mainly due to the increase of the heat energy loss by radiation and thus, the total enthalpy reduced.

Acknowledgments

This work was supported by the Korea Research Foundation Grant funded by the Korean Government (Ministry of Education & Human Resources Development, Basic Research Promotion Fund) (KRF-2006-331-D00089). The authors appreciate the financial support from the Brain Korea 21 Project. The authors would like to acknowledge the support from KISTI (Korea Institute of Science and Technology Information) Supercomputing Center (KSC-2007-S00-1015). The authors would like to especially thank Chul Park at the Korea Advanced Institute of Science and Technology for the offer of his code, which can calculate equilibrium composition and thermodynamic and transport properties.

References

[1] Nicolet, W. E., Shepard, C. E., Clark, K. J., Balakrishnan, A., Kesselring, J. P., Suchsland, K. E., and Reese, J. J., "Analytical and Design Study for a High-Pressure, High-Enthalpy Constricted Arc Heater," Arnold Engineering Development Center, AEDC TR-75-47, July 1975.

[2] Watson, V. R., and Pegot, E. B., "Numerical Calculations for the Characteristics of a Gas Flowing Axially Through a Constrictor Arc," NASA TN D-4042, June 1967.

[3] Smith, A. M. O., and Cebeci, T., "Numerical Solution of the Turbulent Boundary Layer Equations," Douglas Aircraft Division Rept. DAC 33735, May 1967.

[4] Kim, K. H., Rho, O. H., and Park, C., "Navier-Stokes Computation of Flows in Arc Heaters," *Journal of Thermophysics and Heat Transfer*, Vol. 14, No. 2, 2000, pp. 250–258.

[5] Sakai, T., and Olejniczak, J., "Navier-Stokes Computations for Arcjet Flows," AIAA Paper 2001-3014, June 2001.

[6] Sakai, T., and Olejniczak, J., "Improvement in a Navier-Stokes Code for Arc Heater Flows," AIAA Paper 2003-3782, June 2003.

[7] Sakai, T., "Computational Simulation of High Enthalpy Arc Heater Flows," AIAA Paper 2006-1183, June 2006.

[8] Sakai, T., "Computational Simulation of High-Enthalpy Arc Heater Flows," *Journal of Thermophysics and Heat Transfer*, Vol. 21, No. 1, 2007, pp. 77–85.
doi:10.2514/1.26083

[9] Lee, J. I., Kim, C., and Kim, K. H., "Accurate Computations of Arc-Heater Flows Using Two-Equation Turbulence Models," *Journal of Thermophysics and Heat Transfer*, Vol. 21, No. 1, 2007, pp. 67–76.
doi:10.2514/1.25495

[10] Lee, J. I., Kim, C., Kim, K. H., and Rho, O. H., "Investigation of Turbulent Flow Effects in Segmented Arc-Heater," AIAA Paper 2005-172, Jan. 2005.

[11] Lee, J. I., Kim, C., and Kim, K. H., "Numerical Modeling for the Accurate Computations of Arc-Heater Flows," *ECCOMAS CFD 2006 Conference*, Egmond aan Zee, The Netherlands, Sept. 2006.

[12] Jones, W. P., and Launder, B. E., "The Prediction of Laminarization with a Two-Equation Model of Turbulence," *International Journal of Heat and Mass Transfer*, Vol. 15, No. 2, 1972, pp. 301–314.
doi:10.1016/0017-9310(72)90076-2

[13] Terrazas-Salinas, I., and Cornelison, C., "Test Planning Guide for ASF Facilities," Thermophysics Facilities Branch, Space Technology Division, NASA Ames Research Center, A029-9701-XM3 Rev. B, March 1999.

[14] Kim, K. H., Kim, C., and Rho, O. H., "Methods for the Accurate Computations of Hypersonic Flows: 1. AUSMPW+ Scheme," *Journal of Computational Physics*, Vol. 174, Nov. 2001, pp. 38–80.
doi:10.1006/jcph.2001.6873

[15] Jameson, A., and Yoon, S., "Lower-Upper Implicit Schemes with Multiple Grids for the Euler Equations," *AIAA Journal*, Vol. 25, No. 7, 1987, pp. 929–935.

[16] Gordon, S., and McBride, B. J., "Computer Program for Calculation of Complex Chemical Equilibrium Compositions and Applications: 1. Analysis," NASA Reference Publication 1311, Oct. 1994.

[17] Gupta, R. N., Lee, K. P., Thompson, R. A., and Yos, J. M., "Calculations and Curve Fits of Thermodynamics and Transport Properties for Equilibrium Air to 30000 K," NASA RP-1260, Oct. 1991.

[18] Perini, L. L., "Curve Fits of JANAF Thermochemical Data," Applied Physics Lab., ANSP-M-5, Johns Hopkins University, Silver Spring, MD, Sept. 1972.

[19] Srinivasan, S., Tannehill, J. C., and Weilmuenster, K. J., "Simplified Curve Fits for the Thermodynamic Properties of Equilibrium Air," NASA RP-1181, Aug. 1987.

[20] Gupta, R. N., Yos, J. M., Thompson, R. A., and Lee, K. P., "A Review of Reaction Rates and Thermodynamic and Transport Properties for an 11-Species Air Model for Chemical and Thermal Nonequilibrium Calculations to 30000 K," NASA RP-1232, Aug. 1990.

[21] Yos, J. M., "Transport Properties of Nitrogen, Hydrogen, Oxygen, and Air to 30,000 K," AVCO Corp., Tech. Memo. RAD-TM-63-7, March 1963.

[22] Hirschfelder, J. O., Curtiss, C. F., and Bird, R. B., *Molecular Theory of Gases and Liquids*, Wiley, New York, 1967.

[23] Park, C., Jaffe, R. L., and Partridge, H., "Chemical-Kinetic Parameters of Hyperbolic Earth Entry," *Journal of Thermophysics and Heat Transfer*, Vol. 15, No. 1, 2001, pp. 76–90.

[24] Kim, J. G., Oh, J. K., and Park, C., "A High Temperature Elastic Collision Model for DSMC Based on Collision Integrals," AIAA Paper 2006-3803, June 2006.

[25] Murphy, A. B., "Transport Coefficients of Air, Argon-Air, Nitrogen-Air, and Oxygen-Air Plasmas," *Plasma Chemistry and Plasma Processing*, Vol. 15, No. 2, 1995, pp. 279–307.
doi:10.1007/BF01459700

[26] Bacri, J., and Raffanel, S., "Calculation of Transport Coefficients of Air Plasmas," *Plasma Chemistry and Plasma Processing*, Vol. 9, No. 1, 1989, pp. 133–154.
doi:10.1007/BF01015831

[27] Elchinger, M. F., Pateyron, B., Delluc, G., and Fauchais, P., "Radiative and Transport Properties of Some Nitrogen Oxygen Mixtures Including Air," *Proceedings of the 9th International Symposium on Plasma Chemistry*, Vol. I, IUPAC, Pugnochiuso, Italy, 1989, p. 127.

[28] Devoto, R. S., Bauder, U. H., Cailleteau, J., and Shires, E., "Air Transport Coefficients from Electric Arc Measurements," *Physics of Fluids*, Vol. 21, No. 4, 1978, pp. 552–558.
doi:10.1063/1.862261

[29] Asinovsky, E. I., Kirillin, A. V., Pakhomov, E. P., and Shabashov, V. I., "Experimental Investigation of Transport Properties of Low-Temperature Plasma by Means of Electric Arc," *Proceedings of the IEEE*, Vol. 59, No. 4, 1971, pp. 592–601.

[30] Schreiber, P. W., Hunter, A. M., II, and Benedetto, K. R., "Electrical Conductivity and Total Emission Coefficient of Air Plasma," *AIAA Journal*, Vol. 11, June 1973, pp. 815–821.

[31] Capitelli, M., Colonna, G., Gorse, C., and D'Angola, A., "Transport Properties of High Temperature Air in Local Thermodynamics Equilibrium," *The European Physical Journal D*, Vol. 11, No. 2, 2000, pp. 279–289.

[32] Whiting, E. E., Park, C., Liu, Y., Arnold, J. O., and Paterson, J. A., "NEQAIR96, Non-Equilibrium and Equilibrium Radiative Transport and Spectra Program: User Manual," NASA Reference Publication 1389, Dec. 1996.

[33] Park, C., "Calculation of Radiation from Argon Shock Layer," *Journal of Quantitative Spectroscopy and Radiative Transfer*, Vol. 28, July 1982, pp. 29–40.
doi:10.1016/0022-4073(82)90094-2

[34] Wilcox, D. C., *Turbulence Modeling for CFD*, 2nd ed., DCW Industries, La Canada, CA, 1998, pp. 119–122.

[35] Menter, F. R., "Two-Equation Eddy Viscosity Turbulence Models for Engineering Applications," *AIAA Journal*, Vol. 32, Aug. 1994, pp. 1598–1605.

[36] Hightower, T. M., Balboni, J. A., MacDonald, C. L., Anderson, K. F., and Martinez, E. R., "Enthalpy by Energy Balance for Aerodynamic Heating Facility at NASA Ames Research Center Arc Jet Complex," *48th International Instrumentation Symposium*, Instrumentation, Systems, and Automation Society, Research Triangle Park, NC, May 2002.